Triazine-Anion-Based Fluorine-Free Ionic Liquids and Lithium Battery Electrolytes With Flexible Cations

Batteries & Supercaps

Chemistry Europe
European Chemical Societies Publishing

Batteries & Supercaps

RESEARCH ARTICLE OPEN ACCESS

Triazine-Anion-Based Fluorine-Free Ionic Liquids and Lithium Battery Electrolytes With Flexible Cations

Mukhtiar Ahmed[1,2] | Gaurav Tatrari[2] | Alessandro Del Bianco[3] | Paolo Canu[3] | Jyri-Pekka Mikkola[2,4] | Shaikshavali Petnikota[5]

[1]Department of Industrial and Materials Science, Chalmers University of Technology, Gothenburg, Sweden | [2]Technical Chemistry, Department of Chemistry, Chemical-Biological Centre, Umeå University, Umeå, Sweden | [3]Industrial Eng. Dept., University of Padua, Padua, Italy | [4]Industrial Chemistry & Reaction Engineering, John Gadolin Process Chemistry Centre, Åbo Akademi University, Åbo-Turku, Finland | [5]Biomass Technology Centre, Department of Forest Biomaterials and Technology, Swedish University of Agricultural Sciences, Umeå, Sweden

Correspondence: Mukhtiar Ahmed (mukhtiarsjtu@gmail.com,mukhtiar@chalmers.se) | Shaikshavali Petnikota (shaikshavali.petnikota@slu.se)

Received: 19 March 2026 | **Revised:** 18 June 2026 | **Accepted:** 27 June 2026

Keywords: electrolytes | fluorine-free | ionic liquids | lithium metal batteries | triazine

ABSTRACT

Herein, we introduce fluorine-free ionic liquids (ILs) and electrolytes based on electron-deficient triazine, 4,6-Diethoxy-2-Oxo-2H-1,3,5-Triazin-5-ide, (DET), -anion coupled with oligoether-functionalized pyrrolidinium and imidazolium cations. Having the same anion, imidazolium IL show slightly better thermal and electrochemical stabilities, but lower ion transport and higher glass transition temperature, T_g, compared to its pyrrolidinium analog. Doping neat ILs with 20% lithium DET salt and creating lithium-conducting electrolytes increases the overall thermal and electrochemical stabilities but decreases the ion mobilities. As the lithium battery electrolyte, Li||Li symmetric cells confirm stable and reversible Li cycling for both electrolytes, with the imidazolium system showing lower polarization and midpoint hysteresis, indicating faster interfacial kinetics and reduced resistance; correspondingly, it also delivers narrower charge–discharge plateaus and improved voltage stability in Li||LFP half-cells. For imidazolinium-based electrolytes, with the addition of 5 wt% vinylene carbonate (VC), the Li||LFP cells exhibited excellent rate capability from 0.1C to 1C at 60 °C and maintained stable cycling around 200 cycles at 0.1C with nearly 99% capacity retention and coulombic efficiency, demonstrating enhanced interfacial stability and efficient lithium-ion transport.

1 | Introduction

The rapidly increasing global demand for sustainable energy storage systems, driven by the proliferation of electric vehicles, portable electronics, and large-scale renewable energy integration, has intensified the pursuit of rechargeable batteries with higher energy density, and longer life beyond the capabilities of current lithium-ion batteries (LIBs) [1, 2] – motivating the exploration of next-generation battery chemistries. Lithium metal has long been regarded as the most promising anode material for next-generation high-energy batteries owing to its ultrahigh theoretical specific capacity (3860 mAh g^{-1}) and the lowest electrochemical reduction potential (−3.04 V vs. standard hydrogen electrode) [3] – which are highly advantageous for achieving high-voltage and high-energy-density lithium batteries. Despite these merits, the practical application of lithium metal batteries (LMBs) has been severely hindered by critical challenges, particularly safety concerns arising from the use of current state-of-the-art liquid flammable organic-solvent-based electrolytes; thus, electrolyte engineering is crucial, and yet the silver bullet to be discovered [4–6].

A compelling electrolyte paradigm for mitigating these challenges can be lies in the deployment of ionic liquids (ILs)-based electrolytes [7, 8]. Composed exclusively of cationic and anionic species, ILs have negligible to zero vapor pressure

and intrinsic nonflammability, alongside a constellation of physicochemical properties including high ionic conductivity, wide electrochemical stability windows (ESWs), and the capacity to promote the formation of robust and passivating solid–electrolyte interphases (SEI) [9–11]. All these properties together are advantageous for the energy storage devices. Nevertheless, most of the ILs are based on fluorinated anions, mostly based on bis(trifluoromethane)sulfonimide (TFSI) [12, 13], bis(fluorosulfonyl)imide (FSI) [14], and others [15]. This widespread reliance on fluorinated anions possesses critical limitations, compounded by the safety, cost, and limited structural diversity of viable IL anions [16, 17] – a predicament often described as the "*anion crisis*" [18]. Consequently, there exists a significant opportunity to engineer novel fluorine-free anionic frameworks capable of forming low-melting ILs that are weakly coordinating, nonbasic, and non-nucleophilic, while remaining synthetically accessible from inexpensive, readily available precursors [19, 20].

In parallel, strategic cation design particularly the incorporation of ether functionalities [21, 22] – offers a powerful means to modulate ion–ion interactions, reduce lattice energy, and enhance ion mobility [23, 24]. Ether groups introduce conformational flexibility and localized solvation sites, facilitating improved ionic dissociation and transport while simultaneously lowering melting points [25, 26]. Thus, the synergistic optimization of fluorine-free anions and ether-functionalized cations represents a promising design strategy for the development of cost-effective, thermally and hydrolytically stable IL electrolytes with performance characteristics suitable for next-generation LMBs.

In this work, we present two triazine-anion-based ILs with ether-functionalized pyrrolidinium and imidazolinium cations, together with their corresponding lithium-conducting electrolytes formulated via incorporation of 20 mol% lithium DET salt (Figure 1). The triazine anion is anticipated to offer a highly charge-delocalized [27, 28] weakly coordinating environment that mitigates strong ion pairing while preserving wide electrochemical and thermal stability, with its compact heteroaromatic topology expected to favor efficient ion-transport [29]. Simultaneously, the ether substitution within the cationic frameworks disrupts ionic packing, lowers lattice energy and viscosity, and promotes enhanced ionic dissociation, while simultaneously enabling transient Li^+ coordination that facilitates lithium mobility [30]. The electrochemical viability of these fluorine-free IL electrolytes is further evaluated in LMB configurations, providing insight into their compatibility with lithium metal anodes and their ability to support stable interfacial processes under practical operating conditions.

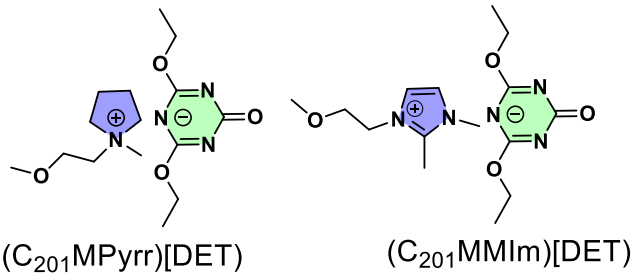

FIGURE 1 | Chemical structures and acronyms of the triazine-anion-based ILs.

2 | Experimental Section

2.1 | Materials

Unless otherwise stated, all commercial reagents were used without any additional purification. 1,2-dimethylimidazole (ACS reagents, >97% purity), *n*-methylpyrrolidine (ACS reagents, >97% purity), 2-bromoethyl methyl ether (99%), silver(I) oxide (>99.9% purity), cyanuric chloride (99% purity), *N*-methyl-2-pyrrolidone (NMP) (anhydrous, 99.5% purity), polyvinylidene fluoride (PVDF) (>99% purity), and activated carbon were all purchased from Sigma–Aldrich. Sodium sulfate (anhydrous, 99% purity), potassium hydroxide, dichloromethane (DCM) (96% purity), tert.butanol (≥99.5%, GC), diethyl ether (99% purity), and ethanol (96% purity) were purchased from VWR (BDH) chemicals. Battery-grade aluminum foil was purchased from Cambridge Energy Solutions Ltd.

2.2 | Synthesis

The synthesis of the targeted triazine-anion-based fluorine-free ILs was accomplished through the multistep synthetic protocol (Scheme 1), with each stage described in detail below. The triazine anion precursor, 2-hydroxy-4,6-diethoxy-1,3,5-triazine (DETOH), recently synthesized and reported by some of us [28].

Methyl ether bromide salts of 1,2-dimethylimidazole and *N*-methylpyrrolidine (0.10 mol each) were dissolved separately in deionized water (50 mL). Silver(I) oxide (6.4 g, 0.055 mol) was added portionwise to each solution under continuous stirring, resulting in the formation of a biphasic reaction mixture. The suspension was stirred at room temperature for 3 h to facilitate halide abstraction and generation of the corresponding hydroxide intermediates. Upon completion, monitored with thin-layer chromatography (TLC), the reaction mixtures were filtered to remove precipitated silver bromide and unreacted silver oxide. To the clear filtrates, DETOH (18.5 g, 0.10 mol) was added gradually over a period of 1 h, ensuring controlled neutralization and salt formation. The resulting mixtures were stirred at ambient temperature for an additional 5 h, after which they were extracted with dichloromethane. The combined organic phases were dried over anhydrous sodium sulfate, filtered, and concentrated under reduced pressure to yield viscous oils. The crude products were further purified by repeated washing with diethyl ether (3×) and subsequently dried under high vacuum at 80 °C for a minimum of 4 days to afford the corresponding ether-functionalized ILs.

2.2.1 | 1-(2-Methoxyethyl)-1-Methylpyrrolidinium-4,6-Diethoxy-2-Oxo-2H-1,3,5-Triazin-5-ide, (C_{201}MPyrr)(DET)

Pale yellow oily liquid at room temperature; ^{1}H NMR (400 MHz, $CDCl_3$) δ: 4.26 (q, J = 2 Hz, 4H), 3.78–3.73 (m, 6H), 3.70–3.64 (m, 2H), 3.27 (s, 3H), 3.15 (s, 3H), 2.14–2.10 (m, 4H), 1.62–1.23

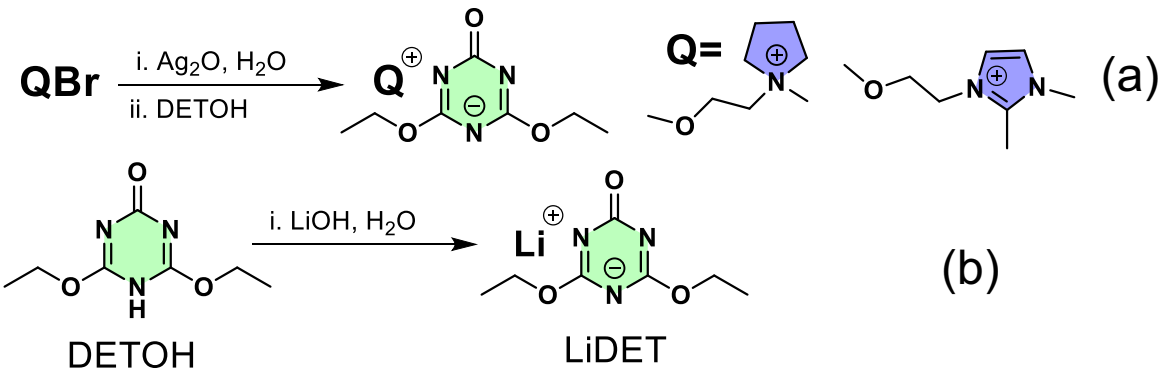

SCHEME 1 | Synthesis of targeted ILs (a) and LiDET (b).

(t, J = 2 Hz, 3H). ^{13}C NMR (100 MHz, $CDCl_3$) δ: 171.96, 171.89, 66.79, 65,27, 63.01, 62.29, 58.89, 48.64, 21.40, 14.58 ppm.

2.2.2 | 3-(2-Methoxyethyl)−1,2-Dimethyl-1H-Imidazol-3-Ium-4,6-Diethoxy-2-Oxo-2H-1,3,5-Triazin-5-ide, (C_{201}MMImd)(DET)

Colorless oily liquid at room temperature. ^{1}H NMR (400 MHz, $CDCl_3$) δ, 7.55 (d, J ≈ 5–6 Hz, 1H), 7.45 (d, J ≈ 5–6 Hz, 1H), 4.58–4.41 (m, 2H), 4.03 (m, 4H), 3.8 (s, 3H), 3.88–3.32 (m, 2H), 2.67 (s, 3H), 1.30 (t, J ≈ 7 Hz, 6H). ^{13}C NMR (100 MHz, $CDCl_3$) δ: 171.65, 170.27, 144.55, 122.70, 121.79, 70.62, 62.22, 58.23, 48.76, 35.55, 50.3, 14.58, 10.24 ppm.

2.2.3 | Synthesis of Lithium 4,6-Diethoxy-2-Oxo-2H-1,3,5-Triazin-5-ide (LiDET)

An aqueous solution of lithium hydroxide (55 mmol in 20 mL of H_2O) was dropped into a stirred aqueous solution of DETOH (55 mmol, 10.18 g). The reaction mixture was stirred at room temperature until the solid material in the aqueous phase completely disappeared, which required ca. 4 h. The progress of the reaction was concurrently monitored by TLC. Upon completion of the reaction, the water was removed under reduced pressure using a rotary evaporator, and the crude product was washed three times with 50 mL portions of diethyl ether to remove unreacted organic impurities. The resulting white solid product was dried under vacuum at 80 °C for at least 4 days to yield the LiDET as a white crystalline solid (>90%). ^{1}H NMR (400 MHz, DMSO-d_6) δ: 4.20–4.15 (q, 4H, CH_2), 1.21–1.18 (t, 6H, CH_3) ppm. ^{13}C NMR (100 MHz, DMSO-d_6) δ: 171.79, 171.79, 63.66, 13.57 ppm.

2.3 | Electrolyte Formulation

Prior to electrolyte preparation, LiDET and the ILs were dried at 80 °C under vacuum overnight, followed by further drying at 100 °C for at least 72 h, and transferred into an argon-filled glovebox (Mbraun, Germany, with H_2O < 0.5 ppm and O_2 < 0.5 ppm). The electrolytes were prepared by doping 20 mol% LiDET to the corresponding neat ILs under stirring until a transparent and homogeneous solution was obtained. For imidazole-based electrolytes, we added 5 wt% vinylene carbonate (VC) as the additive. Prior to each electrochemical measurement, the samples were kept in a vacuum oven at 80 °C for at least 4 days. Water contents were determined by Karl Fischer titration using a Metrohm 917 Coulometer located inside the glovebox.

2.4 | Nuclear Magnetic Resonance (NMR) Spectroscopy

The structures and purity of all synthesized intermediates and ILs were confirmed using a Bruker Ascend Aeon WB 400 NMR spectrometer, Bruker BioSpin AG, Fällanden, Switzerland, with operating frequencies of 400.21 MHz for ^{1}H and 100.64 MHz for ^{13}C. Appropriate deuterated solvents were employed for sample preparation, and the acquired spectra were processed using Bruker TopSpin 3.5 software.

2.5 | Thermal Analysis

Thermal properties were evaluated by using thermogravimetric analysis (TGA) and differential scanning calorimetry (DSC). TGA measurements were carried out on a PerkinElmer TGA 8000 under a nitrogen atmosphere. Samples (2–4 mg) were heated at a rate of 10 °C min^{-1} and the decomposition onset temperature (T_{onset}) was determined from the weight-loss curves using Pyris software. Thermal transitions were further examined by DSC using a PerkinElmer DSC 6000. Samples (2–5 mg) were sealed in aluminum pans and subjected to heating and cooling cycles at 5 °C min^{-1} under the dry nitrogen flow (20 mL min^{-1}). The glass transition temperature (T_g) was obtained from the midpoint of the S-shaped transition in the DSC curves using Pyris software.

2.6 | Pulsed-Field-Gradient (PFG) NMR Diffusometry

PFG NMR diffusometry measurements were carried out on a Bruker Ascend/Aeon WB 400 spectrometer (Bruker BioSpin AG) operating at 400.27 MHz for ^{1}H and 155.56 MHz for ^{7}Li. A Diff50 PFG probe (Bruker) with a maximum gradient strength of 29.73 T m^{-1} was employed. Samples were loaded into standard 5 mm NMR tubes and sealed with plastic caps to prevent air exposure. Prior to measurement, samples were equilibrated at the desired temperature for 30 min.

Self-diffusion coefficients were determined using the stimulated-echo (StE) pulse sequence. The diffusion decay of the NMR

signal intensity, obtained from the Fourier-transformed stimulated echo, was analyzed as a function of the applied gradient strength. For a simple nonassociating liquid, the signal attenuation is described by the Stejskal–Tanner equation (Equation (1)) [31]:

$$A(g, \delta, t_d) = A(0) \exp\left(-\gamma^2 g^2 \delta^2 D t_d \right) \quad (1)$$

where $A(0)$ is the factor proportional to the proton content in the system, and to spin-lattice and spin–spin relaxation times, γ is the gyromagnetic ratio for a used nucleus; g and δ are the amplitude and duration of the gradient pulse; td is the diffusion time; and D is the self-diffusion coefficient. t_d was in the range 4–100 ms for 1H diffusion and 5–15 ms for 7Li diffusion. No diffusion time dependence was observed in these measurements.

2.7 | FTIR Spectroscopy

Attenuated total reflectance-fourier transform infrared (ATR-FTIR) spectra were recorded using a Bruker IFS 80v spectrometer equipped with a deuterated triglycine sulfate (DTGS) detector and a diamond ATR accessory. Spectra were collected in double-sided forward–backward acquisition mode with 256 co-added scans at a spectral resolution of 4 cm^{-1}.

2.8 | Electrochemical Characterization

Electrochemical measurements were carried out using a Metrohm Autolab PGSTAT302N workstation equipped with an FRA32M module and controlled by Nova 2.02 software. Approximately 70 µL of each sample was loaded into a TSC 70 electrochemical cell connected to a Microcell HC temperature controller (RHD Instruments, Germany). Prior to all measurements, the electrodes were polished with 0.25 µm Kemet diamond paste, and the cell was allowed to thermally equilibrate for 10 min.

Linear sweep voltammetry (LSV) was performed in a three-electrode configuration using a 2 mm diameter glassy carbon (GC) wire as the working electrode, a platinum crucible as both counter electrode and sample holder, and an Ag/AgCl-coated silver wire as a pseudo-reference electrode. Anodic and cathodic scans were recorded at a scan rate of 1 mV s^{-1} at 20 °C. All potentials were internally calibrated against ferrocene (Fc), and the ESW was determined using a cut-off current density of 0.1 mA cm^{-2}.

Ionic conductivity was measured by electrochemical impedance spectroscopy (EIS) in a two-electrode configuration (GC working electrode and platinum crucible counter electrode/sample holder) over a frequency range of 1 Hz to 1 MHz with an AC amplitude of 10 mV. Measurements were conducted during heating and cooling cycles between −20 and 100 °C. The cell constant (K_{cell} = 1.701 cm^{-1}) was calibrated using a 100 µS cm^{-1} KCl standard solution.

2.9 | Cell Fabrication

Li||Li symmetric cells were assembled in stainless steel 316L CR2032 coin-type hardware using lithium metal discs (16 mm diameter) as both working and counter electrodes. Whatman GF/D glass microfiber filters (Cytiva; 19 mm diameter) were employed as separators, and 150 µL of electrolyte was introduced into each cell. EIS was performed over a frequency range of 1 MHz to 10 mHz with a 5 mV AC perturbation.

Li||LFP half-cells were fabricated following an analogous protocol. The $LiFePO_4$ (LFP) cathode was prepared via the doctor-blade technique. The electrode slurry comprised LFP (active material), Super P Carbon (conductive agent), and poly(vinylidene fluoride) (PVDF, binder) in an 80:10:10 weight ratio, dispersed in NMP. The uniform slurry was cast onto an aluminum foil current collector and dried under vacuum at 80 °C overnight. Subsequently, circular electrodes (14 mm diameter) were punched from the dried laminate. All electrochemical measurements were conducted using a VMP-3, BioLogic SP-150e potentiostat, and a BioLogic BSC800 battery cycler for galvanostatic charge–discharge measurements.

3 | Results and Discussion

We start with the synthesis and comprehensive structural characterization of the ILs and corresponding electrolytes, followed by a detailed investigation of their thermal properties and culminating with in-depth battery-relevant performance metrics, including ionic conductivity, electrochemical stability, and lithium stripping/plating tests with Li||Li symmetric cells and Li||LFP cells.

3.1 | Basic of Synthesis and Structural Characterization

The ILs and LiDET were synthesized *via* a multistep synthetic protocol (Schemes 1) [28]. In the first step, TCT was converted to TET via nucleophilic substitution with ethanol at ca. 0 °C under basic medium. The resultant TET is subsequently transformed into DETOH through selective hydrolysis with KOH. In the final step, DETOH is neutralized either with an equimolar amount of the cationic hydroxide precursor – generated independently via the reaction of silver oxide with the corresponding bromide salts [32] – to furnish the target ILs, or with lithium hydroxide to yield the LiDET salt. This synthetic strategy provides a scalable, green, and structurally versatile pathway toward next-generation fluorine-free ILs and electrolytes.

All the intermediates, ILs, and lithium salt are characterized by multinuclear (^1H and ^{13}C) NMR spectroscopy (Figures S1–S6). First, the ethoxy chain of the anion exhibits distinct ^1H-NMR signals – the methyl group appears as a triplet at ca. 1.2–1.3 ppm, while the methylene protons appear as a quadruplet at ca. 4.3 ppm. These signals are complemented by the ^{13}C-NMR resonances at ca. 15–16 ppm for the methyl carbon and ca. 60–65 ppm for the methylene carbon. Second, the cationic moieties display characteristic ^1H-NMR signals: for the (C_{201}MMIm)(DET), the methyl groups at C-2 and C-3 positions resonate at ca. 2.7 and 3.3 ppm, respectively; the side ether chain protons appear as triplets at ca. 3.7 and 4.4 ppm and a singlet at ca. 3.9 ppm; and the aromatic imidazolium protons resonate at 7.5–7.6 ppm. For the (C_{201}MPyrr)(DET), the ring protons furthest from nitrogen

give a multiplet at ca. 2.2 ppm, while the methyl groups bonded to nitrogen and to the ether oxygen appear at ca. 3.1 and 3.3 ppm, respectively; the ether chain methylene protons resonate as a triplet at 3.6 ppm and a multiplet at ca. 3.7 ppm. ^{13}C-NMR signals further confirm the successful formation and high purity of the synthesized ILs.

For LiDET (Figure S5), with deprotonation, the disappearance of the broad acidic-proton signal in the ^{1}H NMR spectrum, together with the appearance of two distinct carbonyl-derived ^{13}C resonances at ca. 171 ppm, confirms successful deprotonation of the DETOH intermediate and formation of the targeted LiDET salt.

3.2 | Thermal Properties

All ILs and electrolytes showed single-step decomposition – indicating that both anion and cation degrade within a similar temperature range – and weight loss occurs within the range of ca. 200–250 °C (Figure 2a and Table 1). Yet with proviso, these stabilities may be slightly overestimated, as only isothermal TGA can assess accurate long-term thermal stabilities [33, 34]. For the neat ILs, having the same DET anion, the imidazolium-based IL displays a higher decomposition temperature, which is expected and consistent with the literature [35, 36] and can be related to the aromatic structure of the imidazolium and its tendency to form more packed structures.

The doping of LiDET, as expected and reported, slightly increases the decomposition temperature for both electrolytes compared to their neat ILs [37, 38], and can be attributed to stronger ionic interactions and ionic aggregates, making the lattice more difficult to break and decompose [38]. Overall thermal stability of theses ILs and electrolytes is somehow comparable with the other fluorine-free ILs [39, 40] and electrolytes but bit at lower side when compared to their fluorinated analogs [41, 42], and

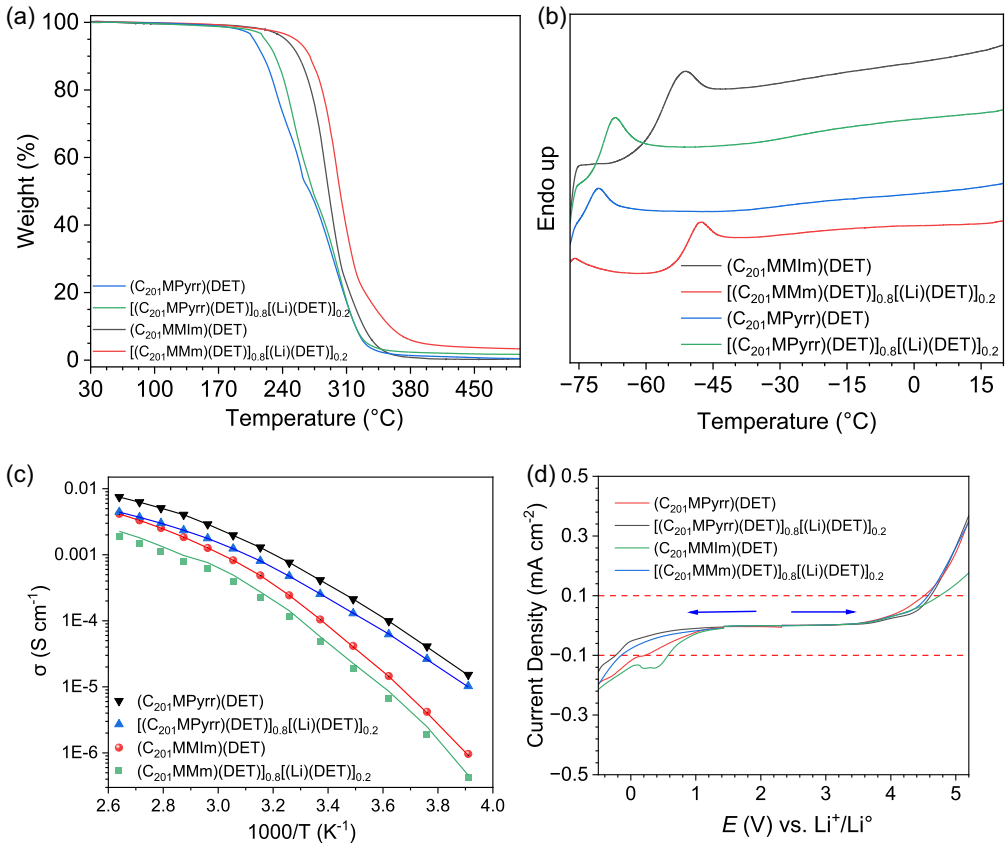

FIGURE 2 | TGA plots (a) DSC traces (b), ionic conductivity (c), and LSV (d) of the neat ILs and the electrolytes. DSC traces are shifted along *Y*-axis for clarity.

TABLE 1 | Physico-chemical and electrochemical properties of ILs and electrolytes.[a]

System	Water content (±5 ppm)	T_g, °C	T_d, °C	σ at 30 °C, S cm^{-1}	ESW, V
$(C_{201}MPyrr)(DET)$	32	−74	206	7.6×10^{-4}	4.3
$[(C_{201}MPyrr)(DET)]_{0.8}[(Li)(DET)]_{0.2}$	43	−68	217	4.7×10^{-4}	4.8
$(C_{201}MMm)(DET)$	39	−57	239	2.4×10^{-4}	4.2
$[(C_{201}MMm)(DET)]_{0.8}[(Li)(DET)]_{0.2}$	49	−52	274	1.1×10^{-4}	4.7

[a]T_m: melting temperature, T_g: glass transition temperature, T_d: decomposition temperature, σ: ionic conductivity.

even higher when compare to carbonated standard lithium-(ion) liquids electrolytes, i.e LP40, with onset of decomposition as low as ca. 40 °C [42].

The DSC traces reveal that all ILs and electrolytes behave like the glass forming liquids, that is, with absence of crystallization or melting events and only have single T_g, evidenced by the step in the heat flow associated with a variation in the heat capacity corresponding to the glass transition temperature, and suggest the amorphous nature of all these systems and the strong Coulombic and structural disorder that hinder long-range ionic ordering [43] (Figure 2b and Table 1).

For the neat ILs, as expected and reported in the literature, the imidazolium-based IL displays higher T_g relative to its pyrrolidinium analog [44, 45], the trend that can be directly correlated with differences in cation architecture, the planar aromatic framework of the imidazolium cation facilitates more efficient molecular packing and enhanced charge delocalization, which together promote strong π–π stacking interactions between adjacent imidazolium rings as well as favorable π–anion interactions with the aromatic DET anion and these cooperative noncovalent interactions lead to a denser and more rigid ionic network, thereby restricting segmental mobility and requiring greater thermal energy to initiate structural relaxation [46, 47]. In contrast, the saturated, nonaromatic pyrrolidinium cation lacks the ability to participate in π–π interactions and exhibits a more conformationally flexible geometry, resulting in less efficient ionic packing and weaker cohesive forces within the liquid matrix [48].

With the addition of the lithium salts, the glass transition temperature for both electrolytes slightly increase, which can be attributed to enhanced ionic interactions that limit ion mobility and decrease the free volume of the systems, and, thus, higher thermal energy is required to reach the same ionic mobility as for the neat ILs [37, 49].

3.3 | Ionic Conductivity

The ionic conductivity for all the systems shows a monotonous increase with temperature (Figure 2c). Having the same anion, pyrrolidinium-based IL and electrolyte exhibit a higher ionic conductivity across the entire studied temperature range than their imidazolium analogs, which correlates well with the DSC analysis data and again suggests higher ionic interaction in imidazolinium based systems. At low temperatures, this difference in ionic conductivity is more pronounced. This discrepancy, as already described for thermal analysis, is linked to cation structure, by the intrinsic differences in cation architecture, wherein the aromatic imidazolium promote the formation of relatively ordered aggregates, while the saturated and conformationally flexible pyrrolidinium rings favor a more disordered and weakly coordinated ionic network that facilitates greater ion mobility – particularly in the low-temperatures – such that progressive thermal activation disrupts these ion aggregates, increases the population of dissociated charge carriers, and ultimately results in a marked enhancement of ionic conductivity [50, 51].

Consistent with the literature [37, 38], doping lithium salts and creating lithium conductive electrolytes results in slightly lower ionic conductivity compared to their corresponding neat ILs. This difference is attributed to the formation of aggregates and ion pairing, which reduce the overall ion mobility.

Overall, the ionic conductivity of these triazine-anion-based ILs and electrolytes is bit at lower side than that of their fluorinated analogs [15, 52], yet higher than that reported for most other nonfluorinated ILs systems [19, 53]. For example, when compare to saccharine (Sac)-based ILs, reported by some of us [54], these DET-based analog have higher conductivity and true similarly with the electrolytes, where doping 10% lithium salt into the Sac-baes ILs leads to an almost one-order-of-magnitude decrease in conductivity conversely, while these DET-based electrolyte shows less conductivity reduction at 30 °C, which can be attributed due the presence of flexible ethoxy substituents in anion that disrupt ionic crosslinking and suppress extensive aggregation [55].

In more detail, the VFT fitting parameters reveal a slightly higher apparent activation energy for the imidazolinium-based IL (Table S1), and further increases with electrolytes, in good agreement with the DSC results. The obtained T_0 values for all neat ILs and their corresponding electrolytes lie in the range of 206–226 K and closely match the calorimetric T_g determined by DSC, which is in accordance with the empirical approximation for IL-based electrolytes: $T_0/T_g \approx 0.75$ [7].

3.4 | Electrochemical Assessments

To evaluate the ESWs, both cathodic and anodic LSV experiments were performed on GC as a working electrode at 20 °C (Figure 2d and Table 1). Starting with the anodic scans of the ILs, there is an abrupt increase in current density at ca. 4.5 V versus $Li^+/Li°$ associated with oxidative decomposition for (C_{201}MPyrr)(DET), while for (C_{201}MMIm)(DET) it remains a bit at higher voltage, ca. 4.7 V versus $Li^+/Li°$. A similar trend is observed during the cathodic scans, the (C_{201}MPyrr)(Sac) IL reduces at a lower potential than its imidazolium analogs, implying that the ESWs of the imidazolium-based ILs are wider than for the pyrrolidinium-based IL (Table 1).

The ESWs of the corresponding electrolytes are slightly wider relative to their neat ILs, with more pronounced stabilization observed for the pyrrolidinium-based electrolytes, particularly under cathodic polarization, likely due to the formation of a passivating SEI-like interphase on the working electrode arising from preferential anion and Li^+–anion complex decomposition [56]. Overall, these ILs and electrolytes exhibit comparable ESWs with other fluorine-free systems [40, 57, 58] but bit lower when compared with their fluorinated analogs [41].

3.5 | Ionic Interactions

To get additional and the deeper insight into the ion–ion interactions, FTIR spectroscopy was applied, and especially in the regions of the asymmetric and the symmetric stretching bands of the carboxylate group of $(DET)^-$ and ring vibration modes of the cyanurate framework, including coupled C–O–R and C–N vibrations, of the $(DET)^-$ anion, where we expect the most relevant features [28] (Figure 3).

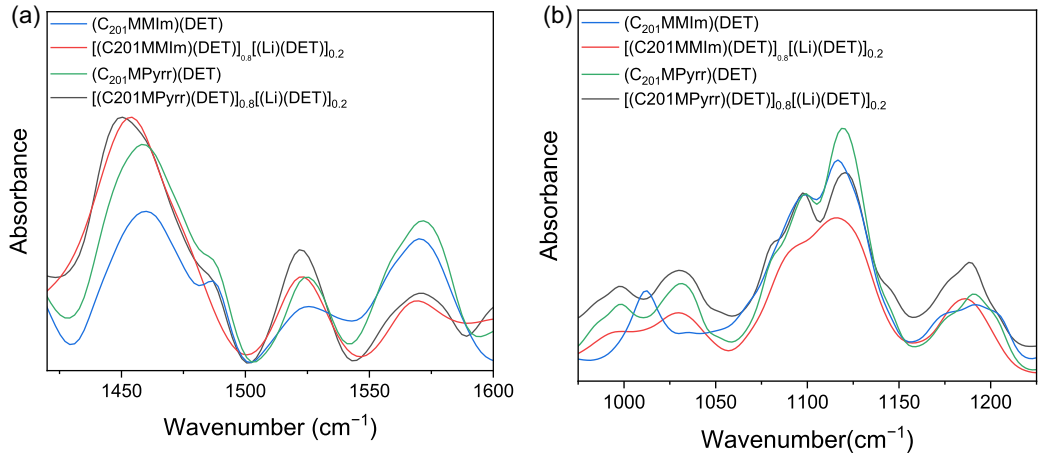

FIGURE 3 | FTIR spectra for the ILs and electrolytes, −CO region (a), C–O–R and C–N (b) region of DET anion.

Start with the asymmetric and symmetric stretching, 1430–1600 cm^{-1}, region; (C_{201}MPyrr)(DET) exhibits the more intense absorption band near 1450–1460 cm^{-1} and a pronounced feature around 1560–1570 cm^{-1}, whereas (C_{201}MIm)(DET) shows broader and less intense bands (Figure 3a). These variations can be attributed to the differing charge distribution of the cations. The aromatic imidazolium cation promotes strong charge delocalization and comparatively localizes the positive charge, resulting in a different ionic organization within the liquid structure, and the saturated pyrrolidinium cation provides stronger cation–anion interactions.

In the 980–1220 cm^{-1} region, (C_{201}MPyrr)(DET) exhibits stronger absorption bands centered around 1100–1120 cm^{-1} compared to the imidazolium analog (Figure 3b); the higher intensity and sharper profile suggest a more ordered local environment around the DET anion. Conversely, (C_{201}MMIm)(DET) displays broader absorption features, indicative of stronger charge delocalization and a wider distribution of ionic conformations arising from the aromatic imidazolium ring. Additional differences are observed near 1000–1040 cm^{-1} and 1180–1200 cm^{-1}, where variations in band intensity further confirm that the nature of the cation influences the vibrational behavior of the DET anion through different electrostatic interactions.

The Li^+ conducting electrolytes produce significant modifications in the FTIR spectra, reflecting substantial changes in the local ionic environment and intermolecular interactions. For the imidazolium system, $[(C_{201}MMIm)(DET)]_{0.8}[(Li)(DET)]_{0.2}$, the addition of Li^+ results in a noticeable decrease in the intensity of the dominant absorption band in the 1100–1120 cm^{-1} region, accompanied by peak broadening and slight frequency shifts. Similar spectral changes are observed for the bands located near 1000–1040 cm^{-1} and 1180–1200 cm^{-1}, indicating that Li^+ strongly coordinates with the DET anion and perturbs its vibrational modes. In the 1430–1600 cm^{-1} region, the absorption band around 1450 cm^{-1} decreases in intensity, while the features between 1520 and 1570 cm^{-1} become broader and less resolved, suggesting a redistribution of electron density within the ionic network because of Li^+–DET complex formation. The broadening of these bands further implies the coexistence of multiple Li^+ coordination environments and solvation structures within the electrolyte. A similar trend is observed for $[(C_{201}MPyrr)(DET)]_{0.8}[(Li)(DET)]_{0.2}$, where Li^+ incorporation causes a reduction in the intensity of the principal band near 1110–1120 cm^{-1} together with significant broadening of neighboring absorption features. Additional modifications in the 1000–1030 cm^{-1} and 1180–1200 cm^{-1} regions confirm that Li^+ coordination strongly influences the vibrational behavior of the DET anion. In the higher wavenumber region (1430–1600 cm^{-1}), the major absorption bands exhibit reduced intensity and altered peak profiles, particularly between 1520 and 1570 cm^{-1}, indicating disruption of the original ionic interactions and the formation of Li^+-coordinated species. Overall, and when compared with the neat ILs, both Li^+-containing electrolytes display broader absorption bands and lower spectral resolution, consistent with increased structural heterogeneity and dynamic ionic rearrangement. A direct comparison of the two systems reveals that although Li^+ coordination affects both electrolytes through similar mechanisms, namely band broadening, intensity reduction, and subtle frequency shifts, the spectral changes are more pronounced in the pyrrolidinium-based electrolyte, especially in the 1100–1120 cm^{-1} and 1450–1570 cm^{-1} regions. This behavior suggests stronger Li^+–anion interactions and a greater degree of ionic network reorganization in the pyrrolidinium system compared with the imidazolium analog [59].

3.6 | Ion Diffusivity

To better understand the transport properties of the neat IL and electrolytes at the molecular level and to gain deeper insight into the relative mobility of the constituent ionic species, ^1H and ^7Li PFG-NMR diffusometry measurements were performed over a broad temperature range (Figure 4). As expected, the self-diffusion coefficients of all ionic species increased monotonically with increasing temperature, reflecting the progressive reduction in viscosity and the enhanced molecular mobility associated with thermally activated transport processes [60]. In the neat ILs, the cationic and anionic species exhibited nearly identical average diffusion coefficients, suggesting a highly correlated mode of ion transport in which both ions move cooperatively through the liquid structure [61]. Owing to the overlap of the corresponding resonances in the NMR spectra, the signals of the individual ions could not be resolved independently; consequently, the experimentally determined diffusion coefficients represent average values arising from the combined motion of both ionic species rather

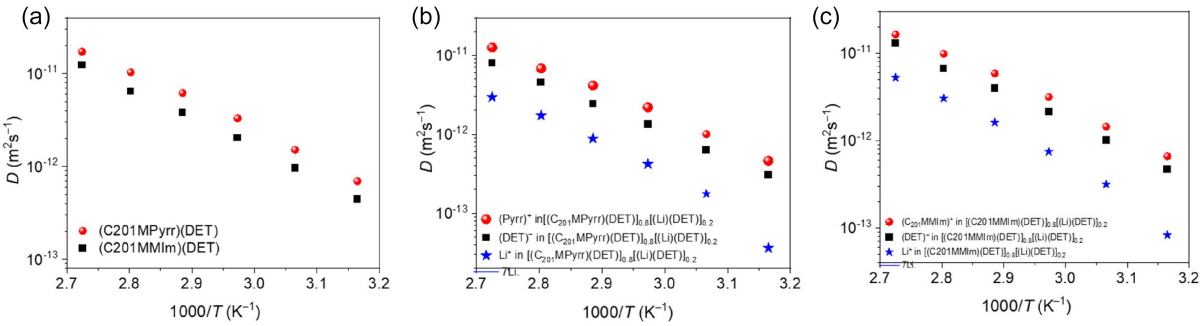

FIGURE 4 | Diffusion coefficients for the neat ILs (a), the $[(C_{201}MPyrr)(DET)]_{0.8}[(Li)(DET)]_{0.2}$ (b) and $[(C_{201}MMIm)(DET)]_{0.8}[(Li)(DET)]_{0.2}$ (c) electrolytes.

than distinct self-diffusion coefficients for the cation and anion. A comparison of the different IL systems further revealed that the pyrrolidinium-based electrolytes exhibit consistently higher self-diffusion coefficients than their imidazolium counterparts (Figure 4a), indicating more facile ion transport within the liquid matrix. Although substitution at the C2 position of the imidazolium ring eliminates the acidic C2–H proton and therefore reduces the propensity for specific hydrogen–bonding interactions, the planar aromatic nature of the imidazolium framework together with the increased steric bulk introduced by substitution. These factors effectively increase the hydrodynamic radius of the diffusing species and hinder translational motion. In contrast, the saturated and nonaromatic pyrrolidinium ring lacks both directional hydrogen-bond donating capability and π–electron interactions, resulting in a less structured ionic environment characterized by greater free volume and weaker, more dynamic cation–anion associations.

Creating Li^+ conducting electrolyte by doping 20 mol% LiDET to the neat ILs, the diffusion of the ionic species becomes significantly altered and decoupled (Figure 4b,c), as the introduction of Li^+ perturbs this dynamic equilibrium, as lithium ions preferentially coordinate with the anions owing to their high charge density and strong Lewis acidity, leading to the formation of Li^+–anion ion pairs and, potentially, larger ionic aggregates [62]. Consequently, the translational freedom of the anions becomes increasingly restricted, resulting in a pronounced decrease in anion diffusivity relative to that of the larger organic cations, which remain comparatively less affected by these coordination interactions and therefore retain higher mobility [63]. This behavior is consistent with the well-established role of lithium–anion coordination in governing the microscopic transport properties of concentrated electrolytes, where the formation of coordinated ionic complexes effectively increases the hydrodynamic size of the diffusing species and suppresses their translational motion [30].

Interestingly, when the diffusion data are considered together with the ionic conductivity measurements, an apparent discrepancy emerges. Although the imidazolium-based electrolytes generally exhibit higher individual diffusion coefficients, they tend to form more structured ionic networks and stronger ion–ion correlations, which promote ionic aggregation and reduce the number of effectively charge-carrying species [64]. Consequently, the higher microscopic mobility observed by PFG-NMR does not directly translate into superior macroscopic ionic conductivity [65]. In contrast, the pyrrolidinium-based electrolytes display lower diffusion coefficients for the individual ionic species, yet exhibit higher ionic conductivities, a behavior that can be attributed to the reduced extent of ionic aggregation, weaker ion correlations, and the more flexible nature of the liquid structure, all of which contribute to more efficient charge transport under an applied electric field [66].

The apparent transference (t_i) for each ion in the electrolytes was calculated from their diffusion coefficients (Di) using equation (2) [67]:

$$ti = \frac{xi \cdot Di}{\sum_i xi \cdot Di} \tag{2}$$

where xi is the molar fraction of each ion. The transference number of a given ionic species, such as lithium ions (Li^+), is defined as the fraction of the total electric current carried by that ion in the electrolyte.

The calculated transference numbers clearly demonstrate that lithium contributes significantly less to the overall ionic transport than the other ions present in the electrolyte (Figure 5). Although Li^+ is intrinsically the smallest ionic species in the system, its mobility is substantially reduced due to its strong coordination with the anions, leading to the formation of Li^+-containing complexes and ionic aggregates. Rather than diffusing as a free ion, lithium is transported as part of these larger coordinated structures, which possess considerably greater effective hydrodynamic sizes and therefore exhibit lower translational mobility. This observation is consistent with the diffusion data discussed previously, where both Li^+ and the coordinating anions displayed lower diffusion coefficients than the organic cations, further supporting the presence of persistent Li^+–anion associations within the electrolyte [68].

The low lithium transference numbers also suggest that a significant fraction of lithium remains involved in strongly coordinated species, including ion pairs and larger aggregates, indicating that complete salt dissociation is not achieved even in the IL environment. Such persistent ionic interactions effectively reduce the number of freely mobile lithium ions available for charge transport and consequently limit the contribution of lithium to the overall conductivity [30]. In contrast, the organic cations and, to a lesser extent, the uncoordinated anions experience fewer transport restrictions and therefore contribute more significantly

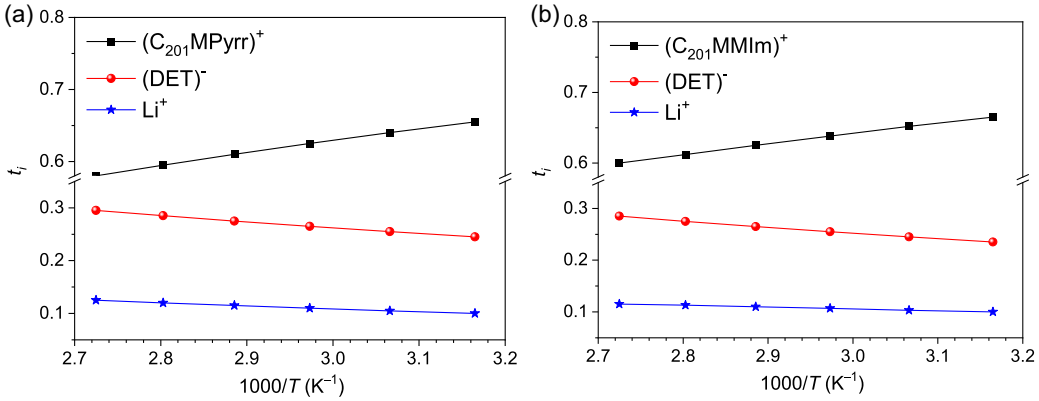

FIGURE 5 | Apparent transference numbers in $[(C_{201}MPyrr)(DET)]_{0.8}[(Li)(Sac)]_{0.2}$ (a) and $[(C_{201}MMIm)(DET)]_{0.8}[(Li)(Sac)]_{0.2}$ (b) as obtained from the PFG-NMR diffusion data.

to the total ionic current [69]. It is, however, important to note that PFG-NMR diffusometry can fundamentally underestimate the diffusion coefficients of charged species, particularly in systems with strong ion pairing and correlated motion, and as a consequence the lithium transference numbers derived from NMR-based diffusion analysis may be systematically lower than those obtained from electrochemical techniques, where the latter can yield values that are typically 2–3 times higher [70, 71].

3.7 | Electrochemical Performance

Turning to the compatibility of the electrolytes with Li metal anodes, the voltage response of $[(C_{201}MPyrr)\ (DET)]_{0.8}[(Li)(DET)]_{0.2}$ and $[(C_{201}MMm)\ (DET)]_{0.8}[(Li)(DET)]_{0.2}$ was evaluated using Li||Li symmetric cells to probe interfacial charge–transfer kinetics and cycling stability (Figure 6). Both electrolytes exhibit highly regular and periodic voltage oscillations over prolonged cycling,

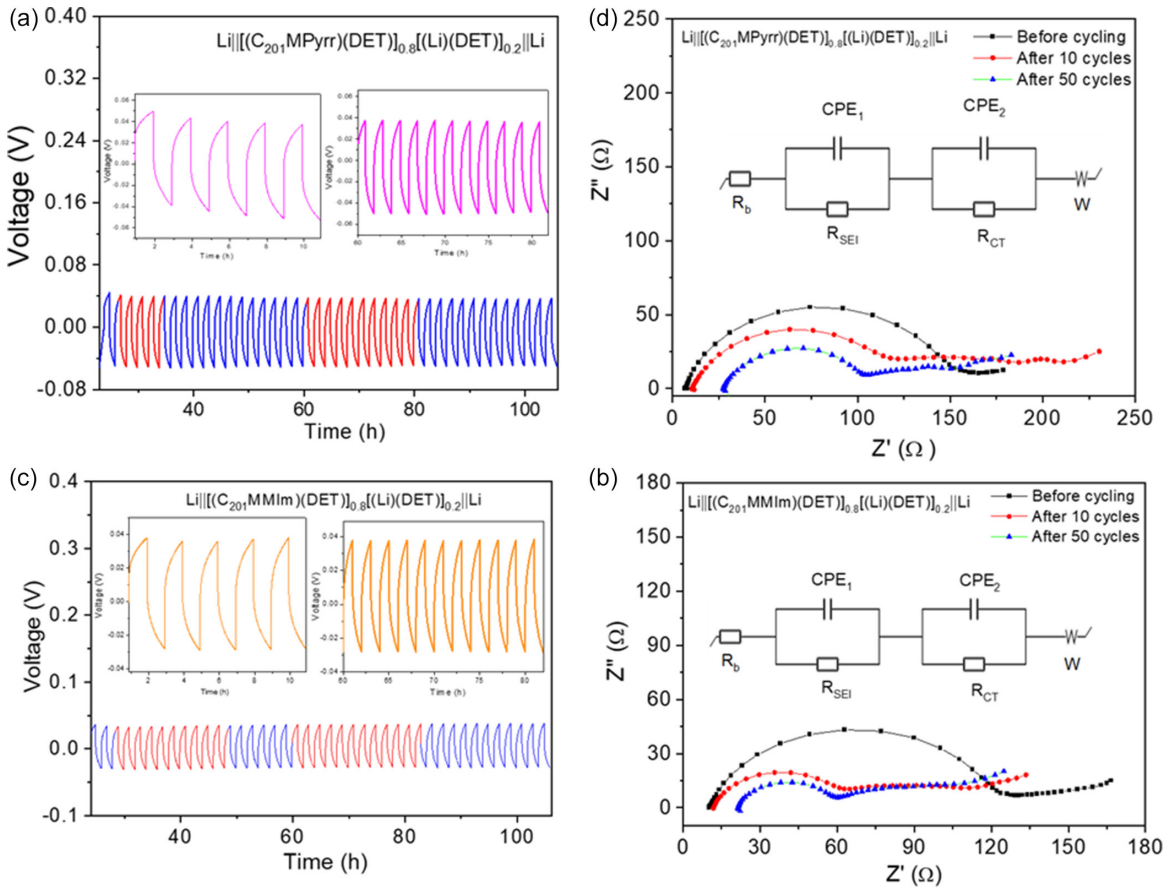

FIGURE 6 | Voltage–time profiles of $Li||[(C_{201}MPyrr)(DET)]_{0.8}[(Li)(DET)]_{0.2}||Li$ (a) and $Li||[(C_{201}MMIm)(DET)]_{0.8}[(Li)(DET)]_{0.2}||Li$ (c) symmetric cells cycled at 0.166 mA cm^{-2} and 30 °C, illustrating the evolution of overpotential during 100 h stripping/plating. Insets enlarge the regions corresponding to early (2–10 h) and extended (60–80 h) cycling. Corresponding Nyquist spectra of $Li||[(C_{201}MPyrr)(DET)]_{0.8}[(Li)(DET)]_{0.8}||Li$ (b) and $Li||[(C_{201}MMIm)(DET)]_{0.8}[(Li)(DET)]_{0.2}||Li$ (d) symmetric cells, collected before cycling and after 10 and 50 cycles.

demonstrating sustained reversibility of Li plating/stripping processes. The absence of progressive voltage increases in polarization confirms stable interfacial electrochemistry and consistent Li^+ transport throughout cycling.

A cycle-resolved quantitative analysis reveals clear differences in interfacial polarization behavior. The imidazolium-based electrolyte, $[(C_{201}MMm)\ (DET)]_{0.8}[(Li)(DET)]_{0.2}$ exhibits lower plating and stripping overpotentials of 18.51 and 24.23 mV, respectively, corresponding to a polarization voltage (ΔV_p) of 42.74 mV and an average overpotential ($\eta_{avg.}$) of 21.37 mV (Figure 6c). In contrast, $[(C_{201}MPyrr)\ (DET)]_{0.8}[(Li)(DET)]_{0.2}$, shows higher plating and stripping overpotentials of 36.47 and 26.50 mV, respectively, resulting in $\eta_{avg.}$ of 31.48 mV and ΔV_p of 62.97 mV (Figure 6a). These increased polarization values indicate comparatively slower interfacial charge–transfer kinetics and higher interfacial resistance in the pyrrolidinium-based electrolyte. The significantly lower polarization of the imidazolium system therefore reflects more favorable Li^+ transport and more facile interfacial charge transfer [72].

In addition to lower polarization, the imidazolium-based electrolyte demonstrates excellent cycle-to-cycle reproducibility, with minimal fluctuation in overpotential over extended cycling, indicating highly uniform Li deposition/dissolution and stable interfacial kinetics. Although the pyrrolidinium electrolyte shows slightly greater variability in overpotential, it remains stable without any progressive increase, confirming sustained reversibility and the absence of cumulative interfacial degradation.

The EIS measurements were performed at different cycling stages (before cycling and after 10 and 50 cycles) for both $Li/[(C_{201}MMm)\ (DET)]_{0.8}[(Li)(DET)]_{0.2}/Li$ and $Li/[(C_{201}MPyrr)\ (DET)]_{0.8}[(Li)(DET)]_{0.2}/Li$ symmetric cells (Figure 6b,d) to evaluate the evolution of bulk and interfacial resistances [73]. Prior to cycling, $[(C_{201}MPyrr)\,(DET)]_{0.8}[(Li)(DET)]_{0.2}$ exhibits a lower bulk resistance (R_b of 7 Ω) than $[(C_{201}MMm)\ (DET)]_{0.8}[(Li)(DET)]_{0.2}$ (R_b of 10 Ω), indicating higher intrinsic ionic conductivity (Figure 6b). However, this advantage is offset by significantly higher interfacial resistances, including R_{SEI} (136 vs. 106 Ω) and R_{ct} (171 vs. 156 Ω), demonstrating greater kinetic barriers for Li^+ desolvation and interfacial charge transfer in the pyrrolidinium-based electrolyte [74]. In contrast, the imidazolium-based electrolyte forms a more kinetically favorable interphase with lower interfacial impedance.

After 10 plating–stripping cycles, $[(C_{201}MMm)\ (DET)]_{0.8}[(Li)(DET)]_{0.2}$ maintains nearly constant bulk resistance (11 Ω) while exhibiting a substantial decrease in charge–transfer resistance (121 Ω) and a marked reduction of the SEI-associated semicircle, indicating rapid formation of a thin, uniform, and ionically conductive interphase that facilitates Li^+ transport and improves interfacial kinetics [75] (Figure 6d). Conversely, $[(C_{201}MPyrr)\ (DET)]_{0.8}[(Li)(DET)]_{0.2}$ undergoes transient interfacial restructuring, reflected by increases in R_b (10 Ω) and R_{ct} (220 Ω), despite a reduction in R_{SEI} (93 Ω), suggesting temporary kinetic limitations associated with SEI reorganization and interfacial stabilization [76].

After prolonged cycling (50 cycles), $[(C_{201}MMm)\ (DET)]_{0.8}[(Li)(DET)]_{0.2}$ sustains low interfacial impedance, with negligible SEI resistance and a further decrease in R_{ct} (103 Ω), confirming the formation of a stable, compact, and highly Li^+–conductive interphase that supports efficient charge transfer and reversible Li plating/stripping [77]. The moderate increase in R_b (20 Ω) is attributed to minor electrolyte aging effects and does not significantly affect overall interfacial kinetics [78]. In contrast, $[(C_{201}MPyrr)\ (DET)]_{0.8}[(Li)(DET)]_{0.2}$ shows gradual interfacial stabilization, with R_{SEI} and R_{ct} decreasing to 71 and 155 Ω, respectively, indicating progressive improvement in interfacial conductivity. However, both bulk and interfacial resistances remain higher than those of the imidazolium-based electrolyte, reflecting comparatively slower interfacial kinetics and greater impedance contributions from electrolyte and interphase evolution.

Overall, despite its initially lower bulk resistance, $[(C_{201}MPyrr)\ (DET)]_{0.8}[(Li)(DET)]_{0.2}$ exhibits consistently higher interfacial impedance and slower kinetic stabilization. In contrast, $[(C_{201}MMm)\ (DET)]_{0.8}[(Li)(DET)]_{0.2}$ undergoes rapid interphase maturation, resulting in lower charge–transfer resistance, improved Li^+ transport, reduced polarization, and superior interfacial stability during extended cycling, consistent with its lower overpotentials and faster interfacial charge–transfer kinetics observed in symmetric cell measurements.

The galvanostatic charge–discharge cycling performance of the LFP cell using the $[(C_{201}MPyrr)(DET)]_{0.8}[(Li)(DET)]_{0.2}$ and $[(C_{201}MPyrr)(DET)]_{0.8}[(Li)(DET)]_{0.2}$ electrolytes exhibit the characteristic flat two-phase plateau associated with the Fe^{2+}/Fe^{3+} redox reaction [79] (Figure 7a–d); however, in direct agreement with the EIS-derived interfacial evolution discussed above, pronounced electrolyte-dependent differences in plateau position, width, and stability are observed. $[(C_{201}MPyrr)(DET)]_{0.8}[(Li)(DET)]_{0.2}$ displays broader and more polarized voltage plateaus, with discharge and charge ranges of 3.3–2.8 V and 3.3–3.9 V, respectively, whereas $[(C_{201}MMIm)(DET)]_{0.8}[(Li)(DET)]_{0.2}$ shows narrower and slightly lower plateaus (3.2–2.7 V during discharge and 3.22–3.7 V during charge), reflecting reduced overpotential and more efficient Li^+ transport [80]. Although both systems retain the intrinsically small hysteresis characteristic of LFP, cycle-resolved analysis reveals that $[(C_{201}MPyrr)(DET)]_{0.8}[(Li)(DET)]_{0.2}$ develops progressively wider charge and discharge plateaus by the 3rd and 4th cycles, consistent with increasing interfacial resistance and slower SEI reorganization, while $[(C_{201}MMIm)(DET)]_{0.8}[(Li)(DET)]_{0.2}$ maintains nearly identical and stable plateau widths across cycles, indicative of a uniform and highly conductive interphase. Correspondingly, Li||LFP cells employing $[(C_{201}MMIm)(DET)]_{0.8}[(Li)(DET)]_{0.2}$ deliver a slightly higher initial discharge capacity (62 mAh g^{-1}) than those using $[(C_{201}MPyrr)(DET)]_{0.8}[(Li)(DET)]_{0.2}$ (56 mAh g^{-1}) at 0.5 C, yet both exhibit rapid capacity fading due to Li-metal kinetic limitations; nevertheless, the narrower voltage spread, lower polarization, and improved capacity retention observed for $[(C_{201}MMIm)\ (DET)]_{0.8}[(Li)(DET)]_{0.8}$ directly correlate with its lower R_{SEI} and R_{ct}, whereas the broader plateaus in $[(C_{201}MPyrr)(DET)]_{0.8}[(Li)(DET)]_{0.2}$ reflect higher interfacial impedance despite its excellent long-term plating–stripping stability.

Overall, and with the initial electrochemical cycling studies confirming that $[(C_{201}MMIm)\ (DET)]_{0.8}[(Li)(DET)]_{0.2}$ enables faster kinetics through rapid SEI stabilization, while $[(C_{201}MPyrr)\ (DET)]_{0.8}[(Li)(DET)]_{0.2}$ prioritizes interfacial robustness at the

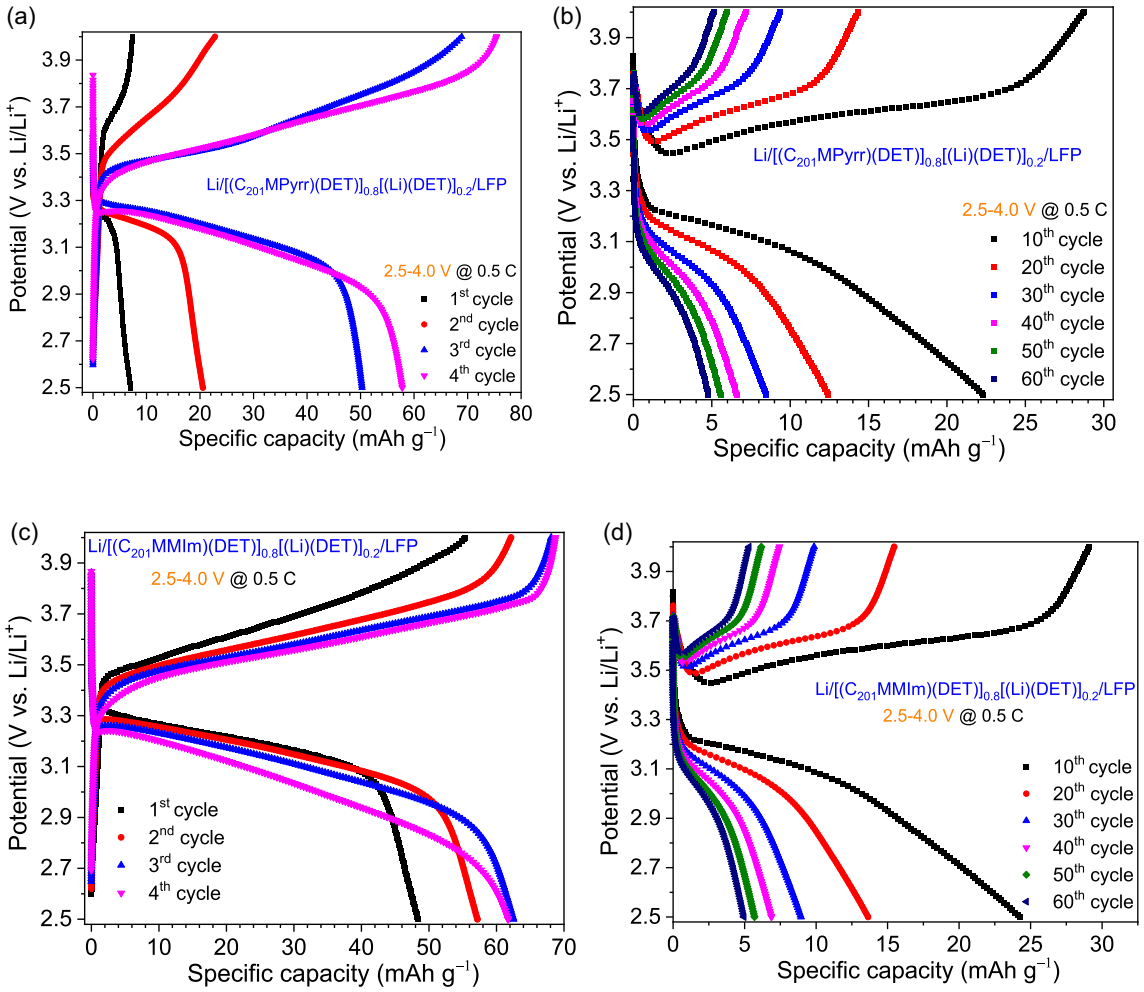

FIGURE 7 | GCPL charge–discharge profiles of Li||[$(C_{201}MPyrr)(DET)]_{0.8}$[$(Li)(DET)]_{0.2}$||LFP cells at 0.5 C and ambient temperature, shown for cycles 1–4 (a), cycles 10–60 (b), and Li||[$(C_{201}MMIm)(DET)]_{0.8}$[$(Li)(DET)]_{0.2}$||LFP cells at 0.5 C and ambient temperature, shown for cycles 1–4 (c) and cycles 10–60 (d).

expense of higher resistance. So we further optimize this electrolyte by adding VC 5 weight%, and cycling at 60 °C, which increases performance significantly.

The Li||[$(C_{201}MMIm)$ $(DET)]_{0.8}$[$(Li)(DET)]_{0.2}$||LFP cells were cycled at progressively increasing current rates from 0.1C to 1C. At 0.1C, the cell delivered its highest discharge capacity of 106 mAh/g, reflecting efficient lithium-ion transport and complete utilization of the active material (Figure 8). With increasing current density, the discharge capacity gradually decreased due to enhanced polarization and reduced time available for lithium-ion diffusion within the electrode and electrolyte. Nevertheless,

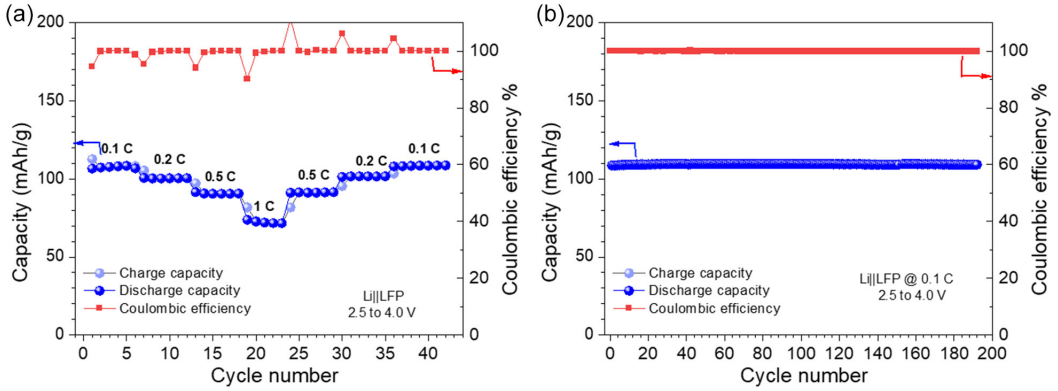

FIGURE 8 | GCPL charge–discharge profiles of Li||[$(C_{201}MMIm)(DET)]_{0.8}$[$(Li)(DET)]_{0.2}$||LFP cell, at different C rates (a), and long cycling at 0.1 C (b) at 60 °C and with 5% VC additive.

the voltage profiles remained well-defined, and the capacity retention at higher rates was maintained, indicating favorable charge–transfer kinetics and sufficient ionic conductivity of the electrolyte. Importantly, when the current rate was returned to 0.1C, the cell recovered most of its initial capacity, demonstrating that the capacity loss at high rates was largely reversible and associated with kinetic limitations rather than irreversible degradation of the electrode/electrolyte interface.

The cell exhibited highly stable cycling behavior over 193 cycles, maintaining the nearly constant discharge capacity with minimal capacity fading. In addition, the coulombic efficiency remained close to 99% throughout the cycling, indicating highly reversible lithium insertion/extraction processes and the suppression of parasitic side reactions. The stable capacity retention over prolonged cycling suggests the formation of a robust electrode/electrolyte interphase that effectively protects both electrodes while allowing efficient lithium-ion transport.

4 | Conclusions

In total, among the ILs, imidazolium-based candidate offer slightly beneficial thermal stability but poorer transport and electrochemical properties; the latter are improved for lithium-doped electrolytes, but the former decrease. Although both electrolytes sustain reversible Li plating/stripping and stable symmetric-cell operation, $[(C_{201}MMIm)(DET)]_{0.8}[(Li)(DET)]_{0.2}$ exhibits more rapid interphase maturation, lower charge–transfer resistance, and reduced polarization, thereby enabling more favorable Li^+ transport and interfacial kinetics than its pyrrolidinium analog. Li||LFP half cells reveal clear kinetic and interfacial differences between the $[(C_{201}MPyrr)(DET)]_{0.8}[(Li)(DET)]_{0.2}$ and $[(C_{201}MMIm)(DET)]_{0.8}[(Li)(DET)]_{0.2}$ electrolytes. Plateau behavior shows that $[(C_{201}MPyrr)(DET)]_{0.8}[(Li)(DET)]_{0.2}$ develops broader charge–discharge spreads across cycles, indicating increasing polarization and slower Li^+ transport, whereas $[(C_{201}MMIm)(DET)]_{0.8}[(Li)(DET)]_{0.2}$ maintains consistently narrow 0.30 V plateaus for both charge and discharge, reflecting stable two-phase behavior and improved charge–transfer kinetics, and with VC additive and at 60 °C it shows very stable cycling at different C rates and long term stability at 0.1 C.

Acknowledgments

The Kempe Foundation, in the memory of J. C. and Seth M. Kempe, is gratefully acknowledged for the financial assistance form GT (grant number JCSMK023−0170, and the equipment grant number: JCSMK23−0090) and so as for MA (grant number JCSMK023−0150). This work is also a part of the activities of the Johan Gadolin Process Chemistry Centre at Åbo Akademi University.

Funding

This study was supported by Kempe Foundation (JCSMK023-0170, JCSMK23-0090, JCSMK023-0150).

Conflicts of Interest

The authors declare no conflicts of interest.

Data Availability Statement

The data that support the findings of this study are available on request from the corresponding author. The data are not publicly available due to privacy or ethical restrictions.

References

1. B. Liu, J.-G. Zhang, and W. Xu, "Advancing Lithium Metal Batteries," *Joule* 2 (2018): 833–845.

2. S. Kim, G. Park, S. J. Lee, et al., "Lithium-Metal Batteries: From Fundamental Research to Industrialization," *Advanced Materials* 35 (2023): 2206625.

3. Q. Wang, B. Liu, Y. Shen, et al., "Confronting the Challenges in Lithium Anodes for Lithium Metal Batteries," *Advanced Science* 8 (2021): 2101111.

4. X. Wang, R. Kerr, F. Chen, et al., "Toward High-Energy-Density Lithium Metal Batteries: Opportunities and Challenges for Solid Organic Electrolytes," *Advanced Materials* 32 (2020): 1905219.

5. S. Dühnen, J. Betz, M. Kolek, R. Schmuch, M. Winter, and T. Placke, "Toward Green Battery Cells: Perspective on Materials and Technologies," *Small Methods* 4 (2020): 2000039.

6. H. Sakaebe, H. Matsumoto, and K. Tatsumi, "Application of Room Temperature Ionic Liquids to Li Batteries," *Electrochimica Acta* 53 (2007): 1048–1054.

7. M. Galiński, A. Lewandowski, and I. Stępniak, "Ionic Liquids as Electrolytes," *Electrochimica Acta* 51 (2006): 5567–5580.

8. A. Lewandowski and A. Świderska-Mocek, "Ionic Liquids as Electrolytes for Li-Ion Batteries—An Overview of Electrochemical Studies," *Journal of Power Sources* 194 (2009): 601–609.

9. C. J. Jafta, X. G. Sun, H. Lyu, et al., "Insight into the Solid Electrolyte Interphase Formation in Bis(fluorosulfonyl)Imide Based Ionic Liquid Electrolytes," *Advanced Functional Materials* 31 (2021): 2008708.

10. M. Y. Yang, S. V. Zybin, T. Das, et al., "Characterization of the Solid Electrolyte Interphase at the Li Metal–Ionic Liquid Interface," *Advanced Energy Materials* 13 (2023): 2202949.

11. S. Zhang, Q. Zhang, Y. Zhang, Z. Chen, M. Watanabe, and Y. Deng, "Beyond Solvents and Electrolytes: Ionic Liquids-based Advanced Functional Materials," *Progress in Materials Science* 77 (2016): 80–124.

12. E. Couadou, J. Jacquemin, H. Galiano, C. Hardacre, and M. Anouti, "A Comparative Study on the Thermophysical Properties for Two Bis[(trifluoromethyl)sulfonyl]imide-Based Ionic Liquids Containing the Trimethyl-Sulfonium or the Trimethyl-Ammonium Cation in Molecular Solvents," *The Journal of Physical Chemistry B* 117 (2013): 1389–1402.

13. T. Sugimoto, Y. Atsumi, M. Kikuta, E. Ishiko, M. Kono, and M. Ishikawa, "Ionic Liquid Electrolyte Systems Based on Bis(fluorosulfonyl)imide for Lithium-Ion Batteries," *Journal of Power Sources* 189 (2009): 802–805.

14. A. Tsurumaki, H. Ohno, S. Panero, and M. A. Navarra, "Novel Bis(fluorosulfonyl)imide-Based and ether-Functionalized Ionic Liquids for Lithium Batteries with Improved Cycling Properties," *Electrochimica Acta* 293 (2019): 160–165.

15. A. B. Pereiro, J. M. Araújo, S. Martinho, et al., "Fluorinated Ionic Liquids: Properties and Applications," *ACS Sustainable Chemistry & Engineering* 1 (2013): 427–439.

16. Y. Wang, X. Yang, Y. Meng, et al., "Fluorine Chemistry in Rechargeable Batteries: Challenges, Progress, and Perspectives," *Chemical Reviews* 124 (2024): 3494–3589.

17. Y. Wang, Z. Wu, F. M. Azad, et al., "Fluorination in Advanced Battery Design," *Nature Reviews Materials* 9 (2024): 119–133.

18. C. A. Angell, Y. Ansari, and Z. Zhao, "Ionic Liquids: Past, Present and Future," *Faraday Discussions* 154 (2012): 9–27.

19. B. Vinay, Y. Nikodimos, T. Agnihotri, et al., "Fluorine-Free Electrolytes in Batteries: Principles, Strategies, and Advances," *Energy & Environmental Science* 18 (2025): 7326–7372.

20. M. Ateia and M. Scheringer, "From "forever Chemicals" to Fluorine-Free Alternatives," *Science* 385 (2024): 256–258.

21. S. Tang, G. A. Baker, and H. Zhao, "Ether- and Alcohol-Functionalized Task-Specific Ionic Liquids: Attractive Properties and Applications," *Chemical Society Reviews* 41 (2012): 4030–4066.

22. H. Ohno, "Functional Design of Ionic Liquids," *Bulletin of the Chemical Society of Japan* 79 (2006): 1665–1680.

23. F. Philippi, D. Rauber, B. Kuttich, et al., "Ether Functionalisation, Ion Conformation and the Optimisation of Macroscopic Properties in Ionic Liquids," *Physical Chemistry Chemical Physics* 22 (2020): 23038–23056.

24. A. Warrington, C. S. Kang, C. Forsyth, et al., "Thermal, Structural and Dynamic Properties of Ionic Liquids and Organic Ionic Plastic Crystals with a Small ether-Functionalised Cation," *Materials Chemistry Frontiers* 6 (2022): 1437–1455.

25. P. Xiao, X. Yun, Y. Chen, et al., "Insights into the Solvation Chemistry in Liquid Electrolytes for Lithium-Based Rechargeable Batteries," *Chemical Society Reviews* 52 (2023): 5255–5316.

26. Y. Li, F. Wu, Y. Li, et al., "Ether-Based Electrolytes for Sodium Ion Batteries," *Chemical Society Reviews* 51 (2022): 4484–4536.

27. N. Luo, Y. F. Ao, D. X. Wang, and Q. Q. Wang, "Putting Anion-π Interactions at Work for Catalysis," *Chemistry–A European Journal* 28 (2022): e202103303.

28. M. Ahmed, G. Tatrari, S. Bhakta, J.-P. Mikkola, and S. Tesfalidet, "New Fluorine-Free Triazine-Anion-Based Ionic Liquids as Supercapacitors Electrolytes," *Journal of Power Sources* 674 (2026): 239760.

29. M. Ahmed, S. S. Rao, A. Filippov, P. Johansson, and F. U. Shah, "Aromatic Heterocyclic Anion Based Ionic Liquids and Electrolytes," *Physical Chemistry Chemical Physics* 25 (2023): 3502–3512.

30. S. Wang, L. Zhang, Z. Hu, et al., "Intrinsic Structural and Coordination Chemistry Insights of Li Salts in Rechargeable Lithium Batteries," *Advanced Materials* 37 (2025): 2420428.

31. J. E. Tanner, "Use of the Stimulated Echo in NMR Diffusion Studies," *The Journal of Chemical Physics* 52 (1970): 2523–2526.

32. S. Pretty, A. Musa, and J. Wren, "Reactions of Bromide and Iodide Ions with Silver Oxide Films on Ag Substrates," *Journal of the Electrochemical Society* 160 (2012): H13–H21.

33. B. Lothenbach, P. Durdzinski, and K. De Weerdt, "Thermogravimetric Analysis," *A Practical Guide to Microstructural Analysis of Cementitious Materials* 1 (2016): 177–211.

34. A. Seeberger, A.-K. Andresen, and A. Jess, "Prediction of Long-Term Stability of Ionic Liquids at Elevated Temperatures by Means of Non-Isothermal Thermogravimetrical Analysis," *Physical Chemistry Chemical Physics* 11 (2009): 9375–9381.

35. Y. Shimizu, Y. Ohte, Y. Yamamura, S. Tsuzuki, and K. Saito, "Comparative Study of Imidazolium- and Pyrrolidinium-Based Ionic Liquids: Thermodynamic Properties," *The Journal of Physical Chemistry B* 116 (2012): 5406–5413.

36. R. L. Gardas, H. F. Costa, M. G. Freire, et al., "Densities and Derived Thermodynamic Properties of Imidazolium-, Pyridinium-, Pyrrolidinium-, and Piperidinium-Based Ionic Liquids," *Journal of Chemical & Engineering Data* 53 (2008): 805–811.

37. J. Pitawala, J.-K. Kim, P. Jacobsson, V. Koch, F. Croce, and A. Matic, "Phase Behaviour, Transport Properties, and Interactions in Li-Salt Doped Ionic Liquids," *Faraday Discussions* 154 (2012): 71–80.

38. L. Aguilera, J. Völkner, A. Labrador, and A. Matic, "The Effect of Lithium Salt Doping on the Nanostructure of Ionic Liquids," *Physical Chemistry Chemical Physics* 17 (2015): 27082–27087.

39. M. Ahmed, A. Kushwaha, A. Filippov, P. Johansson, and F. Ullah Shah, "Saccharinate-Based Ionic Liquids and Lithium Battery Electrolytes," *Batteries & Supercaps* 8 (2025): e202400758.

40. M. Ahmed, A. Filippov, P. Johansson, and F. U. Shah, "Pyrrolidium- and Imidazolium-Based Ionic Liquids and Electrolytes with Flexible Oligoether Anions," *ChemPhysChem* 25 (2024): e202300810.

41. M. Kerner and P. Johansson, "Pyrrolidinium FSI and TFSI-Based Polymerized Ionic Liquids as Electrolytes for High-Temperature Lithium-Ion Batteries," *Batteries* 4 (2018): 10.

42. M. Kerner, N. Plylahan, J. Scheers, and P. Johansson, "Ionic Liquid Based Lithium Battery Electrolytes: Fundamental Benefits of Utilising Both TFSI and FSI Anions?," *Physical Chemistry Chemical Physics* 17 (2015): 19569–19581.

43. E. Gómez, N. Calvar, Á. Domínguez, and E. A. Macedo, "Thermal Behavior and Heat Capacities of Pyrrolidinium-Based Ionic Liquids by DSC," *Fluid Phase Equilibria* 470 (2018): 51–59.

44. C. Chiappe, A. Sanzone, D. Mendola, et al., "Pyrazolium- versus Imidazolium-Based Ionic Liquids: Structure, Dynamics and Physicochemical Properties," *The Journal of Physical Chemistry B* 117 (2013): 668–676.

45. P. Maksym, M. Tarnacka, R. Bielas, et al., "Structure-Property Relationships of Tailored Imidazolium- and Pyrrolidinium-Based Poly(ionic Liquid)s. Solid-Like vs. Gel-Like Systems," *Polymer* 192 (2020): 122262.

46. A. S. Mahadevi and G. N. Sastry, "Cooperativity in Noncovalent Interactions," *Chemical Reviews* 116 (2016): 2775–2825.

47. S. Duan, M. Hua, C. W. Zhang, et al., "Noncovalent Aggregation for Diverse Properties in Hydrogels: A Comprehensive Review," *Chemical Reviews* 125 (2025): 7918–7964.

48. T. Zhou, N. Wang, Y. Gao, and X. Li, "Cation–π Interactions in Polymer Science: From Fundamental Insights to Material Applications," *Polymer Chemistry* 16 (2025): 2058–2074.

49. A. Martinelli, A. Matic, P. Jacobsson, L. Borjesson, A. Fernicola, and B. Scrosati, "Phase Behavior and Ionic Conductivity in Lithium Bis(trifluoromethanesulfonyl)imide-Doped Ionic Liquids of the Pyrrolidinium Cation and Bis(trifluoromethanesulfonyl)imide Anion," *The Journal of Physical Chemistry B* 113 (2009): 11247–11251.

50. Y. Yoshida, O. Baba, and G. Saito, "Ionic Liquids Based on Dicyanamide Anion: Influence of Structural Variations in Cationic Structures on Ionic Conductivity," *The Journal of Physical Chemistry B* 111 (2007): 4742–4749.

51. W. Zheng, A. Mohammed, L. G. Hines Jr, et al., "Effect of Cation Symmetry on the Morphology and Physicochemical Properties of Imidazolium Ionic Liquids," *The Journal of Physical Chemistry B* 115 (2011): 6572–6584.

52. A. Nazet, S. Sokolov, T. Sonnleitner, T. Makino, M. Kanakubo, and R. Buchner, "Densities, Viscosities, and Conductivities of the Imidazolium Ionic Liquids [Emim][Ac], [Emim][FAP], [Bmim][BETI], [Bmim][FSI], [Hmim][TFSI], and [Omim][TFSI]," *Journal of Chemical & Engineering Data* 60 (2015): 2400–2411.

53. I. A. Khan, O. I. Gnezdilov, Y.-L. Wang, A. Filippov, and F. U. Shah, "Effect of Aromaticity in Anion on the Cation–Anion Interactions and Ionic Mobility in Fluorine-Free Ionic Liquids," *The Journal of Physical Chemistry B* 124 (2020): 11962–11973.

54. M. Ahmed, G. Tatrari, P. Johansson, and F. U. Shah, "Sweet Ionic Liquids as High-Temperature and High-Voltage Supercapacitor Electrolytes," *ACS Sustainable Chemistry & Engineering* 12 (2024): 16896–16904.

55. M. Ahmed, S. Bhowmick, A. Filippov, P. Johansson, and F. U. Shah, "Ionic Liquids and Electrolytes with Flexible Aromatic Anions," *Chemistry–A European Journal* 29 (2023): e202301000.

56. A. Wang, S. Kadam, H. Li, S. Shi, and Y. Qi, "Review on Modeling of the Anode Solid Electrolyte Interphase (SEI) for Lithium-Ion Batteries," *NPJ Computational Materials* 4 (2018): 15.

57. X. Mei, Z. Yue, J. Tufts, H. Dunya, and B. K. Mandal, "Synthesis of New Fluorine-Containing Room Temperature Ionic Liquids and Their Physical and Electrochemical Properties," *Journal of Fluorine Chemistry* 212 (2018): 26–37.

58. G. Tatrari, S. Bhakta, M. Ahmed, S. Tesfalidet, and F. U. Shah, "Fluorine-Free Ionic Liquid Electrolytes Featuring Biomass-Derived Heterocyclic Anions for Variable Temperature Supercapacitors," *Advanced Energy and Sustainability Research* 7 (2026): e202500419.

59. F. Castiglione, A. Famulari, G. Raos, et al., "Pyrrolidinium-Based Ionic Liquids Doped with Lithium Salts: How Does Li^+ Coordination Affect Its Diffusivity?," *The Journal of Physical Chemistry B* 118 (2014): 13679–13688.

60. X. Wang, Y. Chi, and T. Mu, "A Review on the Transport Properties of Ionic Liquids," *Journal of Molecular Liquids* 193 (2014): 262–266.

61. R. Hayes, G. G. Warr, and R. Atkin, "Structure and Nanostructure in Ionic Liquids," *Chemical Reviews* 115 (2015): 6357–6426.

62. Q. Lin, D. Kundu, M. Skyllas-Kazacos, et al., "Perspective on Lewis Acid-Base Interactions in Emerging Batteries," *Advanced Materials* 36 (2024): 2406151.

63. S. Horike, D. Umeyama, and S. Kitagawa, "Ion Conductivity and Transport by Porous Coordination Polymers and Metal–organic Frameworks," *Accounts of Chemical Research* 46 (2013): 2376–2384.

64. H. Darjazi, M. Falco, F. Colò, et al., "Electrolytes for Sodium Ion Batteries: The Current Transition From Liquid to Solid and Hybrid Systems," *Advanced Materials* 36 (2024): 2313572.

65. K. S. Han, J. D. Bazak, Y. Chen, et al., "Pulsed Field Gradient Nuclear Magnetic Resonance and Diffusion Analysis in Battery Research," *Chemistry of Materials* 33 (2021): 8562–8590.

66. T. Kato, M. Yoshio, T. Ichikawa, B. Soberats, H. Ohno, and M. Funahashi, "Transport of Ions and Electrons in Nanostructured Liquid Crystals," *Nature Reviews Materials* 2 (2017): 17001.

67. M. Chintapalli, K. Timachova, K. R. Olson, et al., "Relationship between Conductivity, Ion Diffusion, and Transference Number in Perfluoropolyether Electrolytes," *Macromolecules* 49 (2016): 3508–3515.

68. P. Bueno and E. Leite, "Nanostructured Li Ion Insertion Electrodes. 1. Discussion on Fast Transport and Short Path for Ion Diffusion," *The Journal of Physical Chemistry B* 107 (2003): 8868–8877.

69. T. Ueki and M. Watanabe, "Macromolecules in Ionic Liquids: Progress, Challenges, and Opportunities," *Macromolecules* 41 (2008): 3739–3749.

70. A. K. Sethurajan, S. A. Krachkovskiy, I. C. Halalay, G. R. Goward, and B. Protas, "Accurate Characterization of Ion Transport Properties in Binary Symmetric Electrolytes Using In Situ NMR Imaging and Inverse Modeling," *The Journal of Physical Chemistry B* 119 (2015): 12238–12248.

71. G. Pagès, V. Gilard, R. Martino, and M. Malet-Martino, "Pulsed-Field Gradient Nuclear Magnetic Resonance Measurements (PFG NMR) for Diffusion Ordered Spectroscopy (DOSY) Mapping," *The Analyst* 142 (2017): 3771–3796.

72. S. Jeong, V.-C. Ho, O. Kwon, Y. Park, and J. Mun, "High-Stability Room Temperature Ionic Liquids: Enabling Efficient Charge Transfer in Solid-State Batteries by Minimizing Interfacial Resistance," *Energy Materials* 3 (2023): 1–13.

73. T. Pajkossy and R. Jurczakowski, "Electrochemical Impedance Spectroscopy in Interfacial Studies," *Current Opinion in Electrochemistry* 1 (2017): 53–58.

74. H. Tu, K. Peng, J. Xue, et al., "Solvation and Interfacial Chemistry in Ionic Liquid Based Electrolytes toward Rechargeable Lithium-Metal Batteries," *Journal of Materials Chemistry A* 12 (2024): 33362–33391.

75. X. Li, J. Liu, J. He, et al., "Hexafluoroisopropyl Trifluoromethanesulfonate-Driven Easily Li^+ Desolvated Electrolyte to Afford Li‖NCM811 Cells with Efficient Anode/Cathode Electrolyte Interphases," *Advanced Functional Materials* 31 (2021): 2104395.

76. A. Dutta, "Dynamic Processes at the Electrode-Electrolyte Interface: Implications for Lithium Deposition Stability," *ChemElectroChem* 11 (2024): e202400222.

77. Y. Wang, Y. Li, X. Wang, et al., "Shape-Controlled Reversible Li Plating-Stripping for Stable and High-Rate Anode-Free Lithium Metal Batteries," *Advanced Materials* 37 (2025): 2420373.

78. Y. Liao, H. Zhang, Y. Peng, et al., "Electrolyte Degradation During Aging Process of Lithium-Ion Batteries: Mechanisms, Characterization, and Quantitative Analysis," *Advanced Energy Materials* 14 (2024): 2304295.

79. C. Wang, W. Wu, J. Wang, et al., "Application of Advanced Characterization Techniques for Lithium Iron Phosphate: Paving the Way for an In-Depth Understanding of Operation and Fading Mechanisms," *The Journal of Physical Chemistry C* 128 (2024): 21627–21648.

80. C. Hu, M. Geng, H. Yang, et al., "A Review of Capacity Fade Mechanism and Promotion Strategies for Lithium Iron Phosphate Batteries," *Coatings* 14 (2024): 832.

Supporting Information

Additional supporting information can be found online in the Supporting Information section.